Engineering Geology 265 (2020) 105429

Contents lists available at ScienceDirect

Engineering Geology

journal homepage: www.elsevier.com/locate/enggeo

A full description of generalized drag in mixture mass flows

Shiva P. Pudasaini*

University of Bonn, Institute of Geosciences, Geophysics Section, Meckenheimer Allee 176, D-53115 Bonn, Germany

ABSTRACT

Drag plays an important role in the dynamics of mixture mass flows composed of viscous fluid and solid particles. Such flows often take place in environmental and engineering problems. We have analytically derived an enhanced generalized drag that completely describes the drag for any solid volume fraction in mixture mass flows. This provides a full analytical solution and physical basis for the dynamically evolving complex drag. Previous drag formulations were restricted, and produced singularities for large values of the solid volume fraction. Our new model removes singularity inherited by existing models. The analytical model shows different behavior for larger and smaller values of the solid volume fraction, and reveals a smooth variation of the drag coefficient as the solid volume fraction evolves during the flow. Dense to dilute distribution of particles in the mixture, mass flux and material parameters, including particle and fluid densities, characterize the new extended model that strongly determine the drag curve. In contrast to the previous models which tend to show singularity, the most important aspect of the new drag function is that, for any value of the solid fraction, it is sufficiently smooth. We highlight the importance of the new enhanced generalized drag model by comparing it with existing models. A strikingly new understanding is that for some values of the solid volume fraction, the drag takes its maximum, and then, decreases on either side of that particular value. Depending on the dilute to dense flows, two fundamentally different families of asymmetrical drag curves emerge. We have explained the physics behind these special behaviors of drag. With a benchmark simulation, we show that the new enhanced drag offers a great opportunity for the better and full dynamical simulation of a wide range of mixture mass flows. As the new generalized drag reveals many essential physical phenomena, this can be applied in appropriately solving some challenging environmental and engineering problems related to complex multi-phase mixture mass flows including landslide and debris flows.

1. Introduction

Particle-fluid or, bubble-fluid multi-phase mass flow simulation is of great interest in earth science and environmental engineering, and energy science and technology. This includes landslides, debris flows, the nuclear reactors and powerplants (Ganatos et al., 1978; Brennen, 1982; Sangani and Acrivos, 1982a, 1982b; Cook and Harlow, 1984; Durlofsky et al., 1987; Hsu et al., 2003; Absi, 2005; Kolev, 2007; Kowalski, 2008; Luca et al., 2015; Mergili et al., 2017; Pudasaini and Mergili, 2019). In the most often used continuum approaches, the two-phase mixtures are treated as interpenetrating continua with several unknown interfacial terms. These terms contain the transfer of momentum of a phase due to stresses imposed on the phase boundary by the other phases. Various terms are combined in the generalized interfacial forces acting on the dispersed phase (Drew, 1983; Jakobsen et al., 1997; Manninen et al., 1996; Hiltunen et al., 2009; Ishii and Hibiki, 2011; Pudasaini, 2012). This includes buoyancy, the viscous drag, the virtual mass force, the Basset force, and the lift force. Modelling interactions between liquid-particle, or liquid-gas, requires interfacial models for momentum transfer at their interface (Drew, 1983; Ishii and Mishima, 1984; Kendoush, 2008) that pose substantial difficulty.

Any theory that aims to describe the dynamics of a system of particles dispersed in a fluid medium must address the issue of the hydrodynamic interactions among particles. Drag is perhaps the most important hydrodynamic interaction force in mixture flows, that acts at the particle-fluid interface as interfacial momentum exchange (Ganatos et al., 1978; Sangani and Acrivos, 1982a; Sangani and Acrivos, 1982b). This is why in many technical and applied engineering problems, mainly the drag force is considered (Zhang and Yin, 2013; Mergili et al., 2017; Bout et al., 2018; Han et al., 2018; He et al., 2018; Ren et al., 2018).

Two-phase granular-fluid mixture flows, such as landslides, debris flows and hyperconcentrated floods are characterized primarily by the relative motion and interaction between the solid and fluid phases (Drew, 1983; Pitman and Le, 2005; Pudasaini, 2012; de Haas et al., 2015). In natural debris flows, the solid and fluid phase velocities may deviate substantially from each other, essentially affecting the entire flow field (Bout et al., 2018; Mergili et al., 2018a; Yang et al., 2018; Zheng et al., 2018; Qiao et al., 2019; Wang et al., 2019a, 2019b). Depending on the flow configuration and the material involved, several additional physical mechanisms are introduced. Drag is one of the very basic and important mechanisms of two-phase mass flow as it incorporates coupling between the phases. Depending on the amount of

* Corresponding author.
E-mail address: pudasaini@geo.uni-bonn.de.

https://doi.org/10.1016/j.enggeo.2019.105429
Received 25 June 2019; Received in revised form 18 November 2019; Accepted 19 November 2019
Available online 23 November 2019
0013-7952/

grains and the state of flow, Pudasaini (2012) proposed that drag should combine the solid- and fluid-like contributions, and developed a new analytical, generalized drag coefficient that can be applied to a wide range of problems from the simple linear drag to quadratic drag. This drag coefficient is expressed explicitly in terms of essential physical parameters, for example, the volume fractions of the solid and fluid, the solid and fluid densities, terminal velocity of solid particles, particle diameter, and fluid viscosity. This model has recently been extensively used in simulations of complex mass flows including several large natural landslides, avalanches and debris flow events involving process chains and cascades (Kafle et al., 2016, 2019; Kattel et al., 2016, 2018; Bout et al., 2018; Khattri and Pudasaini, 2018; Mergili et al., 2017, 2018b; Pokhrel et al., 2018; Qiao et al., 2019).

The drag can vary substantially depending on the flow dynamics and the concentration of particles. For a dispersed (or, dilute) flow regime, the drag force is relatively well-understood and the analysis is easier. Different constitutive equations and models are presented for the drag force. Theoretically, it has been shown that for increasing particle concentrations, the drag coefficient increases (Ganatos et al., 1978; Sangani and Acrivos, 1982a, 1982b; Durlofsky et al., 1987). However, the problem becomes increasingly complex as the solid volume fraction of the dispersed particle-phase increases (Pitman and Le, 2005; Ishii and Hibiki, 2011; Pudasaini, 2012).

Usually the drag coefficient is a function of the particle concentration and particle Reynolds number (Drew, 1983). However, the drag descriptions based on the Reynolds number also contain non-physical behavior. For vanishing solid fraction, the interfacial drag is equal to zero. On the contrary, as the solid fraction tends to unity, the Reynolds number approaches zero, and the drag becomes infinitely large (Ni and Beckermann, 1991), showing a non-physical or singular behavior. Experimental data show that the drag coefficient increases as the Reynolds number decreases (Brennen, 2005), but, does not show exponential behavior. For a viscous regime, the drag coefficient increases with an increasing volumetric solid concentration (Ishii and Chawla, 1979; Ishii and Hibiki, 2011). However, some models predict that as the flow approaches the Newton's regime, the drag coefficient may increase rapidly even at relatively low (20%) solid fraction and tends to become infinity already at about 50% solid volume fraction (Ishii and Chawla, 1979). This is not realistic. Furthermore, singularities also appear in the simple (Pitman and Le, 2005; Pailha and Pouliquen, 2009) and the generalized (Pudasaini, 2012) drag coefficients developed for particle-fluid mixture mass flows, such as landslides, debris flows and hyperconcentrated floods.

Sangani and Acrivos (1982a, 1982b) developed drag models as a function of the volume fraction of arrays of cylinders, both for dilute and very concentrated distributions of the cylinder. Bossis and Brady (1984) developed a general molecular-dynamics-like method for simulating the dynamics of suspensions of hydrodynamically interacting particles. Durlofsky et al. (1987) presented a general method for computing the hydrodynamic interactions (particularly the drag) for discrete suspended many-particle system, under the condition of vanishingly small particle Reynolds number. However, non of these drag models are complete and smoothly cover the entire domain of the particle concentrations as a single, well defined, analytical model. Such a model is lacking, but could legitimately describe the drag phenomena in a unified way. Here, we develop such a unique drag model.

So, although existing models are mostly applicable to relatively small solid volume fractions, from the structural point of view, drag coefficients increase monotonically as a function of solid volume fraction (Ganatos et al., 1978; Sangani and Acrivos, 1982a, 1982b; Durlofsky et al., 1987; Pitman and Le, 2005; Pailha and Pouliquen, 2009; Pudasaini, 2012). As the particle volume fraction tends to unity, the drag appears to increase exponentially. Which, however, is not realistic, because no real hydrodynamic force can approach infinity. So, either the existing models do not include the whole range of the solid fraction distribution, i.e., the mixture from dilute to dense, or these models tend to show singularity (Ganatos et al., 1978; Sangani and Acrivos, 1982a, 1982b; Durlofsky et al., 1987; Pitman and Le, 2005; Pailha and Pouliquen, 2009; Pudasaini, 2012). Furthermore, mostly some empirical values have been used in practice for different types of mass flows, for both dilute and dense mixture of particles and fluid (Zwinger et al., 2003; Pudasaini and Hutter, 2007), which, however, might be questionable as such values lack physical ground.

Thus, modelling of the drag force is still a largely unsolved problem in science and engineering as there is no consensus on it, mainly for the complex particle-fluid mixture flows such as landslides, avalanches, debris flows, and hyperconcentrated flows. The main challenge that still remains is the construction of a suitable constitutive equation or, a unified model for the drag coefficient, that covers the whole spectrum of the flow dynamics. So, a drag coefficient model that covers the entire distribution of the solid particle concentration is needed. The major concern is the modelling of the drag force coefficient of a general nature. Here, we present a simple, enhanced and fully analytical model, without any singularity, for generalized drag coefficient in mixture mass flows consisting of viscous fluid and the solid particles that covers the entire domain of the solid volume fraction. The model is sufficiently smooth and bounded, with its maximum lying realistically somewhere between the dilute to dense limits of particles. Comparison of the new drag model with some existing drag models reveals a much better physical basis and performance of the new model. We also apply the new drag model to simple mass flow simulations to show the fundamental differences between the new and old drag models. This highlights the essence and application potential of the new drag model to complex and real flow situations such as landslides, avalanches and debris flows.

2. Importance of proper description of drag in mass flow simulation

Generally, high fluid content or pore-fluid pressure is the main cause of the triggering and high mobility of landslides. High water content presents a great challenge in simulating mass flows. Such flows can be better simulated with the two-phase particle-fluid mixture mass flow model (Pudasaini, 2012) that includes generalized drag (Mergili et al., 2017, 2018a, 2018b; Bout et al., 2018; Qiao et al., 2019). Drag is one of the most essential aspect of the complex interactions between the solid particles and viscous fluid in two-phase mass flow, because it influences the relative motion between the two phases. Because the drag firmly depends on whether the flow is dilute or dense, the flow dynamics, extent of deposition and travel distance is strongly controlled by the state and different formulations of drag.

When a huge and rapid landslide impacts a reservoir and turns into a subaqueous multi-phase particle-fluid mixture flow, the drag between particles and viscous fluid plays important role in the overall dynamics (Zhang and Yin, 2013; Bout et al., 2018; He et al., 2018; Mergili et al., 2018a, 2018b; Pudasaini and Mergili, 2019). In such a situation, the application of properly formulated full description of drag, such as the one proposed here, is essential for the reliable modelling of the complex mixture mass flows that results in a completely different flow dynamical and deposition processes than without or improper drag models, mentioned in the previous section. This is the main aspect of this contribution.

The drag between phases evolves and generally increases with the higher solid volume fraction, and results in increased resistance of the fluid motion. Drag plays central role in the transport processes and flow mobility (Pudasaini, 2012; Pudasaini and Fischer, 2016a; Ren et al., 2018; Zheng et al., 2018) and the development of the solid-dominated frontal surge, lateral levee formation, and phase-separation between solid particles and viscous fluid in debris flows and deposition (de Haas et al., 2015; Pudasaini and Fischer, 2016b; Wang et al., 2019b). As the drag can strongly change the local material composition (Pudasaini and Fischer, 2016b), it directly influences the impact pressure of the

mixture against obstacles (Kattel et al., 2018; Kafle et al., 2019). Furthermore, drag plays crucial role in debris flow erosion (Pudasaini and Fischer, 2016a; Han et al., 2018; Yang et al., 2018). So, appropriate formulation of drag is essential for the proper modelling of phase-separation, erosion, flow mobility, and the reliable engineering design of the defense structures. The enhanced general drag model developed here can be applied to various problems in geophysics, and civil and environmental engineering, such as the dynamic evolution of flow-like avalanches, debris flows, generation of tsunami waves by landslides, and subsequent submarine landslide motions (Mergili et al., 2017; Mergili et al., 2018a, 2018b; Wang et al., 2019a; Pudasaini and Mergili, 2019).

3. Full description of generalized drag

3.1. Model development

First, we define parameters and variables. The suffixes s and f, respectively, denote the solid and fluid constituents in the debris mixture. Let ρ_s and ρ_f are the solid and fluid densities, $\gamma = \rho_f/\rho_s$ is the density ratio, and η_f is the fluid viscosity. Let $\mathbf{u}_s = (u_s, v_s, w_s)$ and $\mathbf{u}_f = (u_f, v_f, w_f)$ be the solid and fluid phase velocity fields, α_s and $\alpha_f = (1 - \alpha_s)$ denote the solid and fluid volume fractions in the mixture, d is particle diameter, and g is gravity. Here, we follow the derivation and formulation in Pudasaini (2012). So, the generalized drag coefficient, C_{DG} can be written as:

$$C_{DG} = \alpha_s \alpha_f (\rho_s - \rho_f) g / |\mathbf{u}_f - \mathbf{u}_s|^2. \tag{1}$$

In order to close the drag, we need to construct an expression for the term $|\mathbf{u}_f - \mathbf{u}_s|^2$ in terms of the known physical parameters and the dynamical variables. For this, we consider the mass balance equations for the solid and fluid constituents (Pudasaini, 2012):

$$\frac{\partial \alpha_s}{\partial t} + \nabla\cdot(\alpha_s \mathbf{u}_s) = 0, \tag{2a}$$

$$\frac{\partial \alpha_f}{\partial t} + \nabla\cdot(\alpha_f \mathbf{u}_f) = 0. \tag{2b}$$

Since $\alpha_f = 1 - \alpha_s$, the mass balances in (2) imply that the total mixture is divergence free, i.e., $\nabla \cdot (\alpha_s \mathbf{u}_s + \alpha_f \mathbf{u}_f) = 0$. Thus, the net volume flux must be a constant, say $\mathcal{K}$, such that

$$\alpha_s \mathbf{u}_s + \alpha_f \mathbf{u}_f = \mathcal{K}. \tag{3}$$

Note that here, $\mathcal{K}$ is a vector of three components (constants), obtained by component-wise integration of $\nabla \cdot (\alpha_s \mathbf{u}_s + \alpha_f \mathbf{u}_f) = 0$, which when written in vector form leads to (3). Considering (3) and following Pudasaini (2012), the relative phase velocity in the mixture, $|\mathbf{u}_f - \mathbf{u}_s|$, can be rearranged in terms of the solid and the fluid constituent velocities to get:

$$|\mathbf{u}_f - \mathbf{u}_s| = \frac{1}{\alpha_s}|\mathcal{K} - \mathbf{u}_f| \le \frac{1}{\alpha_s}(|\mathcal{K}| + |\mathbf{u}_f|), \tag{4a}$$

$$|\mathbf{u}_f - \mathbf{u}_s| = \frac{1}{\alpha_f}|\mathcal{K} - \mathbf{u}_s| \le \frac{1}{\alpha_f}(|\mathcal{K}| + |\mathbf{u}_s|). \tag{4b}$$

So, the quantities on the left can be approximated by the (upper bound) quantities on the right in (4a)-(4b). Consider a function or, a parameter $\mathscr{P} \in [0, 1]$ which eventually combines the solid-like and fluid-like drag contributions (discussed below) to flow resistance in two-phase debris flows (Pudasaini, 2012). Multiply (4a) by $\mathscr{P}$ and (4b) by $(1 - \mathscr{P})$ and add to obtain their combination, which when squared leads to a unique expression:

$$|\mathbf{u}_f - \mathbf{u}_s|^2 = \left[\mathscr{P}\frac{1}{\alpha_s}|\mathbf{u}_f| + (1-\mathscr{P})\frac{1}{\alpha_f}|\mathbf{u}_s| + \left\{\left(\frac{\mathscr{P}}{\alpha_s} + \frac{1-\mathscr{P}}{\alpha_f}\right)\mathscr{K}\right\}\right]^2, \tag{5}$$

where $\mathscr{K} = |\mathcal{K}|$, and equality refers to the upper bounds in (4). Until this point, only the fluid dynamical equations are used. Now, we approach some experimental results to model $|\mathbf{u}_s|$ and $|\mathbf{u}_f|$.

For simplicity, consider one-dimensional (near) vertical flows. As in Richardson and Zaki (1954), the magnitude of solid particle velocity can be expressed as

$$|u_s| = \alpha_f^M \, \mathscr{U}_T, \tag{6}$$

where $\mathscr{U}_T$ is the terminal velocity of a particle falling in the fluid, and the parameter $M = M(Re_p)$ depends on the particle Reynolds number $Re_p = \rho_f d \, \mathscr{U}_T/\eta_f$ (Pitman and Le, 2005; Pudasaini, 2012). Equation (6) is mainly applicable for dilute flows where the inter-particle distance is substantially larger than the particle size. This limitation has been removed now by incorporating the relatively dense to dense packing of the solid grains. As we will see later, this is a great advantage of the new enhanced generalized drag model.

Next, consider fluid flow through a relatively dense packing of solid grains, similar to the flow of fluid through the porous medium. Typical fluid velocity under such conditions is represented by (Pailha and Pouliquen, 2009; Pudasaini, 2012):

$$|u_f| = \frac{\gamma}{180}\left(\frac{\alpha_f}{\alpha_s}\right)^3 \alpha_s \, Re_p \, \mathscr{U}_T. \tag{7}$$

Combining (1), (5), (6) and (7), we obtain a new drag coefficient:

$$C_{DG} = \frac{\alpha_s \alpha_f (1-\gamma) g}{\left[\mathscr{U}_T\{\mathscr{P}\mathcal{F}(Re_p) + (1-\mathscr{P})\mathcal{G}(Re_p)\} + \left(\frac{\mathscr{P}}{\alpha_s} + \frac{1-\mathscr{P}}{\alpha_f}\right)\mathscr{K}\right]^j}, \tag{8}$$

where $\mathcal{F} = \gamma(\alpha_f/\alpha_s)^3 Re_p/180$ and $\mathcal{G} = \alpha_f^{M(Re_p)-1}$ are the fluid-like and solid-like drag contributions. As often the other terms in the momentum equations are normalized by the solid density (Pitman and Le, 2005; Pudasaini, 2012), we have also normalized the drag in (8) by the solid density. Furthermore, $j = 1$ or 2 correspond to linear (laminar-type) or quadratic (turbulent-type) drag coefficients.

The quantity

$$\mathscr{S}_{\mathscr{P}}(\alpha_s) = \left(\frac{\mathscr{P}}{\alpha_s} + \frac{1-\mathscr{P}}{\alpha_f}\right)\mathscr{K}, \tag{9}$$

in the drag expression (8) is called the smoothing or the damping function. The emergence of $\mathscr{S}_{\mathscr{P}}$ in (8) is very important as it removes the singularity from the existing drag coefficient. This will be made clear in Section 4.2. That $\mathscr{S}_{\mathscr{P}}$ incorporates the contribution due to the mass flux (i.e., mass flux intensity) is new as compared to the drag in Pudasaini (2012), where a particular value of $\mathscr{K} \approx 0$ was assumed, and thus $\mathscr{S}_{\mathscr{P}} = 0$ in the previous consideration. The choice $\mathscr{K} = 0$ was restricted to the regions where velocities are relatively small. This, however, is not realistic in general. As it will be clear in the sequel, this restriction produced singularity in the drag for large values of the solid volume fraction (Pitman and Le, 2005; Pailha and Pouliquen, 2009; Pudasaini, 2012). Furthermore, in the previous consideration, $\mathscr{P}$ was just a pure numerical parameter in the domain between 0 and 1 (Pudasaini, 2012; Mergili et al., 2017, 2018a, 2018b). But, as we will see in Section 3.3.2, here we present (construct) a functional relation for $\mathscr{P}$ on α_s.

So, the general functional relation of $\mathscr{P}$ on α_s, and the emergence of $\mathscr{S}_{\mathscr{P}}$ in (8) via (9) is crucial for the general structure of the enhanced drag that is smooth, and systematically, and mechanically legitimately removes the singularity. Equation (8) is called the enhanced generalized drag in mixture mass flows. This fully describes the drag for any values of the solid volume fraction α_s.

3.2. Different contributions in enhanced drag

There are three distinct contributions in the enhanced generalized

drag (8), mainly in it's denominator. The first and second components associated with $\mathscr{F}$ and $\mathscr{G}$ depend largely on the material composition, but also on the flow dynamics. However, the new contribution, called the smoothing function $\mathscr{S}_{\mathscr{P}}$, associated with $\mathscr{K}$, depends on the mass flux. This is the dynamical quantity. The dynamics associated with $\mathscr{F}$, $\mathscr{G}$ and $\mathscr{K}$ has been elaborated in Section 4.7. An important aspect of the $\mathscr{K}$ term in (8) is that there is a strong coupling between the mass flux and the drag. The drag is high as mass flux is low, and vice versa. Particularly important is the flow transition to the run-out zone and deposition. In such a scenario, the velocity, and thus the mass flux, decreases quickly, so does $\mathscr{K}$. This results in rapid increase in the drag that enhances the mass halting. This will be made clear at Section 4.3, and Fig. 4. Such a dynamical coupling between the mass flux and the drag is novel, and appears to be quite natural as it is derived from the first principle.

3.3. The closures

$\mathscr{K}$ and $\mathscr{P}$ can play crucial role in the full dynamical model calibration and validation (Mergili et al., 2017; Bout et al., 2018; Qiao et al., 2019). So, next, we need to model $\mathscr{K}$ and $\mathscr{P}$.

3.3.1. The closure for the mass flux contribution $\mathscr{K}$

The dynamics of $\mathscr{K}$ can be complex. There are two possibilities. Either $\mathscr{K}$ can be considered as a suitably chosen parameter, or be formally estimated (or, derived) from the physics of the flow. As $\mathscr{K}$ depends on the total mass flux, this in turn depends on the flow dynamics, i.e., the flow velocities and volume fractions of the solid and fluid constituents in the mixture. So, a typical value of $\mathscr{K}$ can be obtained from (3).

There can be different options to model $\mathscr{K}$. Here, we present one possible method. By assuming a velocity drift λ (a real number), we can establish a relationship between $\mathbf{u}_s$ and $\mathbf{u}_f$, $\mathbf{u}_f = \lambda \mathbf{u}_s$ (Pokhrel et al., 2018; Khattri and Pudasaini, 2018). However, λ is equal to unity if there is no relative velocity between the phases, but, in general, can deviate away from unity. Depending on whether the fluid phase is faster or slower than the solid phase, λ would be greater than or smaller than unity. Now, with the notation $|\mathbf{u}_s| = \mathscr{U}_s$, the magnitude of $\mathbf{u}_s$, (the upper bound of) $\mathscr{K}$ can be estimated from (3):

$$\mathscr{K} \leq \alpha_s|\mathbf{u}_s| + \alpha_f|\mathbf{u}_f| \;\; = \alpha_s|\mathbf{u}_s| + \lambda\alpha_f|\mathbf{u}_s| \;\; = (\alpha_s + \lambda\alpha_f)\mathscr{U}_s. \tag{10}$$

The form of $\mathscr{K}$ in (10) is important and is determined by the mass flux $(\alpha_s + \lambda\alpha_f)\mathscr{U}_s$.

In natural debris flows, the velocity can be of the order of 10 ms^{-1}, and the solid volume fraction is about 0.6, a typical value for a saturated debris material. Thus, (10), or (3) implies that $\mathscr{K} \approx 10.0$ ms^{-1}. Furthermore, as $\mathscr{U}_T$ is proportional to the flow velocity, similar ordering as of $\mathscr{K}$ can also be obtained for $\mathscr{U}_T$.

3.3.2. The closure for $\mathscr{P}$

As an important dynamical variable (or, parameter), $\mathscr{P}$ covers different spectrum of mass flows ranging from the limiting dilute to dense flows. Different forms of $\mathscr{P}$ can emerge from different flow dynamics. As discussed in Section 3.1, $\mathscr{P}$ combines the solid-like and fluid-like drags in the mixture. Such combinations can be linear or non-linear in the domain $[0,1]$. In Pudasaini (2012), only a simple situation was considered by assuming a typical numerical value of $\mathscr{P}$ in the domain $[0, 1]$. However, as $\alpha_s \in [0,1]$, this dynamical variable can be utilized to construct the possible functional relations for $\mathscr{P}$, this is important. So, we represent $\mathscr{P}$ as a general function of α_s; typically, $\mathscr{P} = \alpha_s^n$, because ${\alpha_s}^n \in [0,1]$, where n is a positive number. This consideration is novel. As n decreases, $\mathscr{P}$ increases, so does the drag, because increase in $\mathscr{P}$ is associated with the more dense flows (Pudasaini, 2012). The most probable candidates for n are the values of order unity.

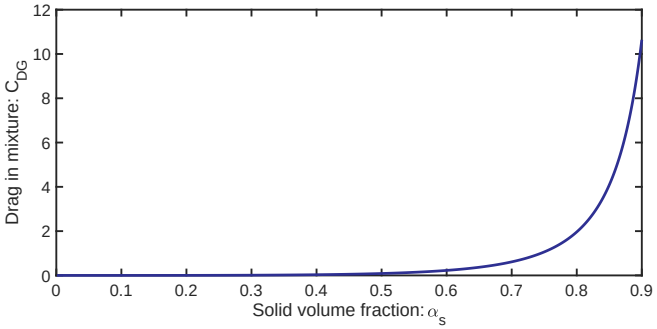

Fig. 1. The generalized drag in mixture flow for $\mathscr{K} = 0$ showing the very rapid and unphysical increase for the larger solid volume fraction.

4. The dynamics of the enhanced generalized drag

Now, we analyze the dynamics of the new enhanced generalized drag (8) in terms of α_s. Except otherwise stated, following the above discussion, we choose the parameter values as $(\rho_s, \rho_f, M, \mathscr{K}, \mathscr{U}_T, Re_p, j, g) = (2700,1300,3.0,10.0,10.0,1000,1.0,9.81)$, with appropriate dimensions. These parameter choices are reasonable, and can be explained by the underlying physics of the flow (Richardson and Zaki, 1954; Pitman and Le, 2005; Pudasaini, 2012; Mergili et al., 2017, 2018a, 2018b).

4.1. Singularities in the existing models

First, we choose $\mathscr{P} = 0.5$, representing a typical debris mixture, and $\mathscr{K} = 0$ (Pudasaini, 2012; Mergili et al., 2017, 2018b). Fig. 1 shows how the drag can tend to unrealistically large value as the solid volume fraction becomes large for this choice of $\mathscr{K}$. And the drag coefficient tends to infinity as the solid volume fraction tends to unity. This was the limitation (due to singularity) of the drag model presented in Pudasaini (2012). Such singularity also appears in other existing models. See, e.g., Ishii and Chawla (1979), Pitman and Le (2005), Ishii and Hibiki (2011), for different flows including dispersive and bubbly flows, flow of fluid in densely packed granular materials (Pailha and Pouliquen, 2009), and the hydrodynamic models (Ganatos et al., 1978; Sangani and Acrivos, 1982a, 1982b; Durlofsky et al., 1987), which will be discussed in detail in Section 5. This singularity has been removed now by the new model (8) as given below.

4.2. Removal of singularity

Fig. 2 shows how the new generalized drag function (8) removes the singularity that appeared in the existing model with $\mathscr{K} = 0$ already in the dilute regime that increased uncontrollably for solid fraction (α_s) larger than 0.3. This figure shows the direct comparison between the very strongly singular existing drag, without the smoothing function $\mathscr{S}_{\mathscr{P}}$, i.e., $\mathscr{K} = 0$, $\mathscr{P} = 0.5$, and the smooth and well bounded new

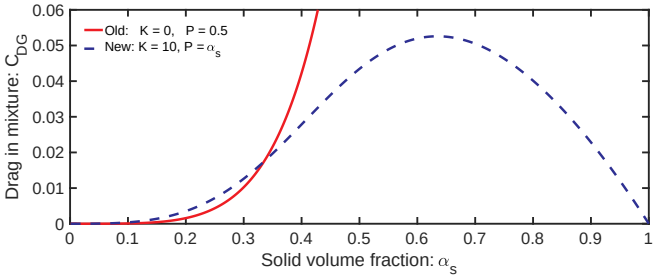

Fig. 2. The generalized drag in mixture flow for $\mathscr{K} \neq 0$ showing how the new enhanced drag removes the singularity from the existing drag with $\mathscr{K} = 0$.

enhanced generalized drag with the corresponding smoothing function $\mathscr{S}_{\mathscr{P}}$, i.e., $\mathscr{K} = 10$, $\mathscr{P} = \alpha_s$. The difference is huge, already in the very dilute to dilute regime, $\alpha_s < 0.4$, and incomparable even in the usual state of the debris mixture, $0.4. < \alpha_s < 0.65$, and one could even not think to compare the old drag with the new drag in the dense regime. The new drag function reveals very smooth and nice behavior for the entire domain, from very dilute to very dense, including the fluid and solid limits, i.e., $\alpha_s \to 0$, $\alpha_s \to 1$, respectively. Importantly, there is no singularity in the new drag in Fig. 2 for any value of α_s. Section 4.7 further justifies the mechanical importance of the new generalized drag.

Several important phenomena are observed. One of the most striking points is that, for the reasonably selected parameter values, as done here, the mean value of the enhanced generalized drag in Fig. 2 is about 0.02. This value is often used in literature for mass flow simulations but without any physical justification, to validate different simulations (Zwinger et al., 2003; Pudasaini and Hutter, 2007). We have provided a full analytical solution and physical basis for the dynamically evolving complex drag in the mixture mass flow with well-posed behavior. So, there is an urgent need to replace physically unbounded drag by the new, well bounded, smooth and regular generalized drag.

4.3. Influence of $\mathscr{K}$

Dynamically, the drag and the mass flux are inversely related. Higher values of $\mathscr{K}$ means higher mass flux, which in turn indicates the lower drag. This is consistent as Fig. 3 shows such effects of $\mathscr{K}$ (for $\mathscr{K} = 10$ and $\mathscr{K} = 15$) on drag for the particular choice of $\mathscr{P} = \alpha_s$. In Section 4.5, we will discuss in detail the choice of the function, or the parameter $\mathscr{P}$ and the dynamics of new generalized drag. As $\mathscr{K}$ is associated with the mass flux, the velocity decreases as the mass flux decreases, and consequently the drag increases rapidly leading to the halting of the mass flow. A small decrease in the mass flux can result in a large to huge increase in the drag. Fig. 4 explains exactly this behavior.

4.4. The smoothing function

As the smoothing function $\mathscr{S}_{\mathscr{P}}$ is of paramount importance in determining the quality of drag (magnitude and form), we analyze it in detail with $\mathscr{P} = \alpha_s^n$, for different n values. Fig. 5 shows that $\alpha_s = 0.5$ is the pivotal point of the smoothing function. For $n \leq 1$, $\mathscr{S}_{\mathscr{P}}$ strongly smoothes or regularizes the drag on the left, and for $n > 1$, it does the same on the right. But, it is clear that the rate of smoothing is completely different on the left and the right of $\alpha_s = 0.5$, and for larger and smaller values of n than unity. So, the functional relation of $\mathscr{P}$ with α_s^n, for different values of n is important. However, the different choices of n in $\mathscr{P} = \alpha_s^n$, and thus in $\mathscr{S}_{\mathscr{P}}$, results in completely different families of drag curves. This will be analyzed in Section 4.5.2, Fig. 7.

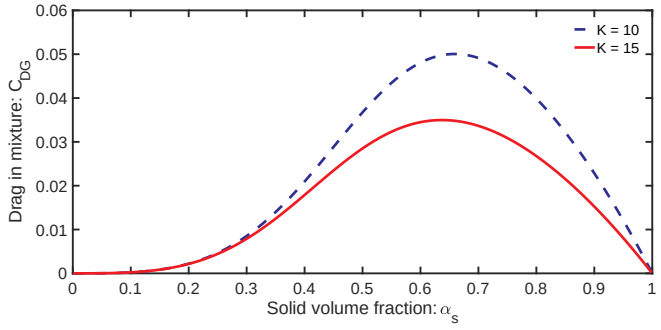

Fig. 3. The enhanced generalized drag in mixture for $\mathscr{P} = \alpha_s$, and for two typical values of $\mathscr{K}$ as the solid volume fraction evolves.

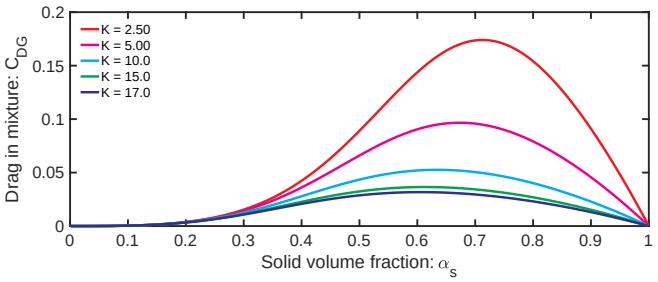

Fig. 4. The enhanced generalized drag in mixture for $\mathscr{P} = \alpha_s$, and different high to low values of $\mathscr{K}$ as the solid volume fraction evolves. This shows how the flux intensity controls the drag.

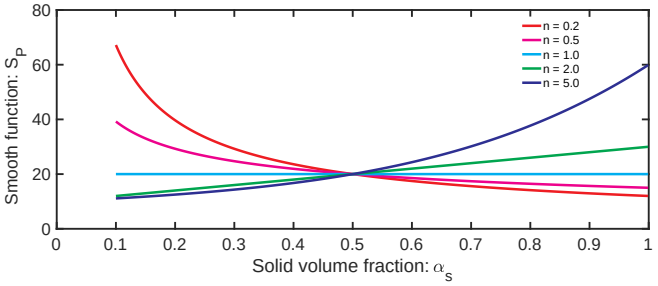

Fig. 5. Depending on the exponent n in $\mathscr{P} = \alpha_s^n$, the function $\mathscr{S}_{\mathscr{P}}$ smoothes the enhanced generalized drag fundamentally differently.

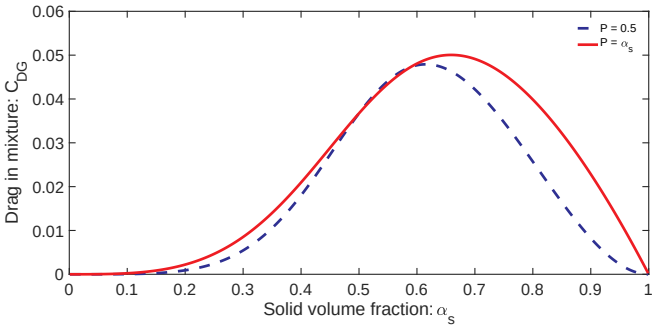

Fig. 6. The enhanced generalized drag in mixture flow with a constant, and variable values of $\mathscr{P}$, $\mathscr{P} = 0.5$ and $\mathscr{P} = \alpha_s$, and $\mathscr{K} = 10$ for both, as the solid volume fraction evolves.

4.5. Influence of $\mathscr{P}$

4.5.1. A parameter or variable $\mathscr{P}$

We present results for a numerical value of $\mathscr{P} = 0.5$ and a variable $\mathscr{P} = \alpha_s$, and $\mathscr{K} = 10$ as shown in Fig. 6 which displays the typical dynamics of the new full and enhanced generalized drag function. This indicates that the model (8) shows different behavior for larger and smaller values of the solid volume fractions. Constant $\mathscr{P}$ produces a bit more symmetrical solution whereas the variable $\mathscr{P}$ produces more asymmetrical result. For both choices of $\mathscr{P}$, this figure shows a very smooth variation of the drag coefficient as the solid volume fraction evolves from its small value to the largest value.

4.5.2. Families of drag curves with different $\mathscr{P}$ functions

Without loss of generality, now we choose $n = 0.1,0.5,1.0,2.0,3.0,5.0$. The resulting drag dynamics are shown in Fig. 7 as a function of the solid volume fraction, and for different n values. There are two interesting and physically important observations. First, with the increasing value of $\mathscr{P}$ (associated with decreasing n), the drag coefficient increases for the larger values of the solid volume fraction (α_s), which,

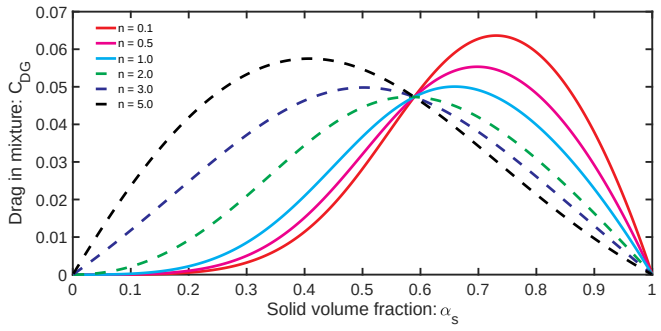

Fig. 7. The enhanced generalized drag in mixture flow with different $\mathscr{P}$ (or, n) values, $\mathscr{P} = \alpha_s^n$, as a function of the solid volume fraction.

however, decreases for the lower values of α_s. This can be explained, because the higher value of $\mathscr{P}$ is associated with the dense flows for which the drag are higher (Pudasaini, 2012; Qiao et al., 2019). The larger ($n > 1$) and smaller ($n < 1$) values of n generate two fundamentally different families of positively and negatively skewed drag curves as indicated by the dashed and solid lines, respectively. Furthermore, with the changing value of $\mathscr{P}$, the quality of the drag curves change as the curves shift to the left or right. For $n > 1.0$ as n increases, the peaks of C_{DG} increase but shift to the left (to lower value of α_s). However, for $n < 1.0$ as n decreases, the peaks of C_{DG} increase, and shift to the right (to higher α_s values). More importantly, for smaller values of $\mathscr{P}$ closer to α_s (i.e., $n = 1.0$), the drag curve tends to become more symmetric, however, for large values of $\mathscr{P}$ (i.e., $n = 0.1$), it becomes strongly asymmetrical with strong variation of the drag value. So, (*i*) better knowledge of $\mathscr{P}$, and (*ii*) evolving solid fraction (Mergili et al., 2017, 2018a, 2018b; Bout et al., 2018; Qiao et al., 2019) is very important for the proper understanding of the drag, and thus, the flow dynamics as a whole.

It is interesting to note that, although $\alpha_s = 0.5$ was the pivotal point for the smoothing function $\mathscr{S}_{\mathscr{P}}$ (Fig. 5), $\alpha_s \approx 0.6$ appears to be the pivotal point for the drag functions in Fig. 7. Such a shift in the pivotal point is determined by the numerator and denominator of C_{GD} in (8), including the three components of the denominator, associated with the $\mathscr{F}$, $\mathscr{G}$, and $\mathscr{K}$ terms.

4.6. Influence of the material parameters

4.6.1. The material densities

The buoyancy reduced normal load of the particles is linearly dependent on the density ratio parameter γ, so does the numerator of C_{DG} in (8). However, C_{DG} varies strongly nonlinearly with γ, because $\mathscr{F}$, that appears in the denominator of C_{DG}, is also a function of γ. Fig. 8 shows that C_{DG} varies strongly and non-linearly, from one C_{DG} curve to another, mainly for larger values of γ, and the overall magnitude of C_{GD} decreases with increasing γ values.

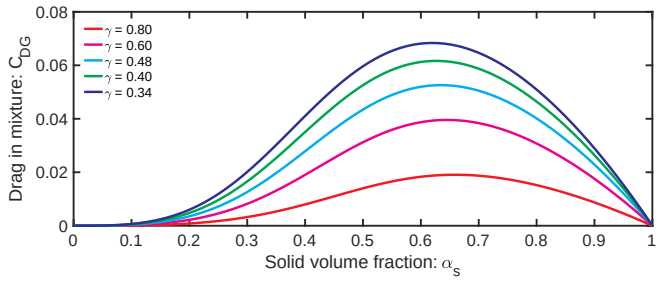

Fig. 8. Non-linear dependence of the enhanced generalized drag on the fluid to solid density ratio γ, as a function of the solid volume fraction.

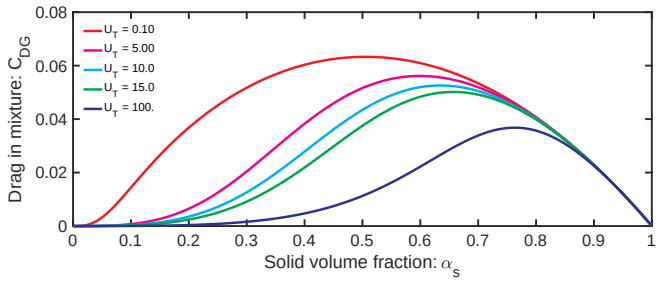

Fig. 9. Dependence of the enhanced generalized drag on $\mathscr{U}_T$.

4.6.2. Effect of the parameter $\mathscr{U}_T$

Even more interesting is the influence of the particle terminal velocity $\mathscr{U}_T$ on the enhanced generalized drag C_{DG}. This has been depicted in Fig. 9. Very big and very small terminal velocities result in completely different drag forces. As $\mathscr{U}_T$ can play the role of a representative velocity, low $\mathscr{U}_T$ values lead to higher drags, and the high $\mathscr{U}_T$ values result in low drags. Measured $\mathscr{U}_T$ value is as high as 380 ms^{-1}, in skydiving (https://www.bbc.com/news/science-environment-19943590). So, the new drag model may also be used in such special flow dynamical simulations. The results in Fig. 9 is consistent with the results in Section 4.3 (Fig. 4), in determining the magnitude of C_{DG}. For very small $\mathscr{U}_T$, the drag is distributed almost normally about the mean value of the solid volume fraction ($\alpha_s = 0.5$). However, for very large $\mathscr{U}_T$, the drag curve skewed strongly negatively. So, the terminal velocity of the particles in the mixture plays important role in determining the form and magnitude of the drag curve.

4.7. Mechanical importance and dominance of $\mathscr{F}$, $\mathscr{G}$ and $\mathscr{K}$ terms

The above results imply that it is important to compare the dynamical behavior and dominance of the three different terms in the denominator of the generalized drag (8). Fig. 10 reveals that the drag corresponding to each of the three terms associated with $\mathscr{F}$, $\mathscr{G}$ and $\mathscr{K}$ (switching the other two terms off) are fundamentally different. On the one hand, the fluid-type drag ($\mathscr{F}$) is the worst one and can not be taken alone, while the solid-type drag ($\mathscr{G}$) is also not acceptable and is unphysical as it increases exponentially already in the dilute regime and cannot be applied both in the intermediate particle concentration and the dense regime, which, however, represents the most of the debris and geophysical mass flows. On the other hand, the drag associated with the mass flux ($\mathscr{K}$) is smooth, behaves very well, and is well bounded for the entire domain of the solid fraction distribution. However, it does not include the material and other flow properties as discussed above. The complete drag structure (denoted by 'All' in Fig. 10) in (8), that includes all three components, is thus necessary to legitimately describe the complex drag associated with the mixture mass flows covering the whole spectrum of the particle concentration. This highlights the mechanical importance of the new enhanced drag in properly modelling the dynamics of mixture mass flows such as

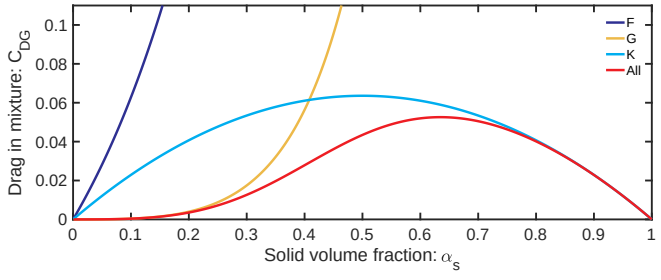

Fig. 10. Comparison of the drag components associated with the fluid-type ($\mathscr{F}$), solid-type ($\mathscr{G}$), and flux ($\mathscr{K}$) terms in the generalized drag; and the entire drag including all three terms ('All') as the solid volume fraction evolves.

landslides and debris flows.

4.8. Non-linear drag

As for the linear drag, families of curves can be obtained for the non-linear or the quadratic drag associated with the turbulence-type flows. This is described by $j = 2$ in (8). However, we must choose the parameter values appropriately. For this, we can select the parameters as: $(\rho_s, \rho_f, M, \mathscr{K}, \mathscr{W}_T, Re_p) = (2700,1100,2.5,4.0,3.0,3500)$. These values are compatible with the turbulence flows (Richardson and Zaki, 1954; Pitman and Le, 2005; Pudasaini, 2012). Qualitatively similar trend as in linear drag (Fig. 7) are observed (not shown). However, the drag magnitudes are much smaller, particularly for $n \geq 1$. This is physically justifiable, because drag varies inversely with the relevant Reynolds number (Brennan, 2001; Brennen, 2005; Ishii and Hibiki, 2011).

Furthermore, the pivotal point shifts a bit to the right for the non-linear drag curves as compared to the linear drag curves. However, the locus of the maxima of the drag curve is fundamentally different than the same for the linear drag. Now, for increasing α_s, the curve drops slowly on the left of the pivotal point, but, afterwards, it rises up exponentially. So, such a locus characterizes the dynamical behavior of the drag curves as a function of $\mathscr{P} = \alpha_s^n$.

5. Comparison with some existing drag models and methods

Fig. 10 compares the partial fluid-type drag model (Pailha and Pouliquen, 2009), solid-type drag model (Pitman and Le, 2005) and the full new model. Similarly, Figs. 1 and 2 compare the previous drag (Pudasaini, 2012) in mixture mass flow indicating the very rapid and unphysical increase for the larger solid volume fraction, and the well behaving new drag in mixture flow. These figures clearly reveal how the existing drag models applied in simulating mixture mass flows contain unphysical singularities for dilute to dense, and very dense mixture flows. The new model, however, removes such singularity.

Here, we further discuss some other pioneering analytical and numerical hydrodynamic drag models presented for the mixture flows. Sangani and Acrivos (1982a) developed numerical drag models as a function of the volume fraction of the cylinders for the slow flow past a square and a hexagonal array of cylinders. Two different models were developed, for dilute and dense (very concentrated) distributions of the cylinder. Their numerical models are shown to be in excellent agreement with the corresponding asymptotic expressions for negligible as well as maximum allowable volume fraction of cylinders.

The analytical models for the drag force (coefficients) developed by Sangani and Acrivos (1982a) for flow past square arrays of cylinders, for dilute and dense flows, respectively, written in non-dimensional form, are,

$$\frac{F_{dilute}}{\mu_f u_f} = \frac{4\pi}{\ln(\alpha_c^{-1/2}) - 0.738 + \alpha_c - 0.887\alpha_c^2 + 2.038\alpha_c^3 + O(\alpha_c^4)}, \quad \alpha_c \leq 0.4, \tag{11}$$

and

$$\frac{F_{dense}}{\mu_f u_f} \approx 9\pi/2\sqrt{2}\left\{1 - \left(\frac{\alpha_c}{\alpha_{c_{max}}}\right)^{1/2}\right\}^{-5/2}, \quad \alpha_{c_{max}} - \alpha_c \ll 1.0, \tag{12}$$

where F_{dilute} and F_{dense} are the applied drag forces in dilute and dense arrangements of cylinders, α_c is the volume fraction of cylinders, and $\alpha_{c_{max}}$ is the corresponding volume fraction when the cylinders are touching each other.

Fig. 11 depicts the comparison between the drag models presented in Sangani and Acrivos (1982a) and the new model (8) with parameters $n = 2.0$, $\mathscr{W}_T = 4.0$, $Re_p = 300$. Due to the lognormal nature of the drag functions in Sangani and Acrivos (1982a), direct comparison between the models therein and the new model presented here is not that easy. So, for the purpose of comparison, the functions are appropriately scaled and plotted in lognormal scale (panel A), or normalized with their respective maximum values (panel B) in Fig. 11 for both drag functions in Sangani and Acrivos (1982a), and our new drag model. However, the numerical and analytical models in Sangani and Acrivos (1982a, 1982b) show fast (or, exponential) increase of the drag forces for $\alpha_c \geq 0.2$. This indicates the singular behavior in their drag models. The models (11) and (12) present different approximate analytical solutions for dilute and dense distributions of cylinders with no analytical connection between them. Both panels show singular behavior of the Sangani and Acrivos (1982a) models already from relatively dilute mixture (i.e., for $\alpha_c \geq 0.2$), but our model is well controlled, smooth, and behaves nicely for any values of the solid volume fraction. There is a substantial jump between those analytical solutions in Sangani and Acrivos (1982a) around $\alpha_c = 0.2$. The numerical solution has also been presented by Sangani and Acrivos (1982a) for the entire dilute domain ($\alpha_c \leq 0.4$). However, both the analytical and numerical solutions therein tend to show exponential increase of the drag force as the flow change from very dilute to dilute regime. We note that, analogous analytical and numerical models are presented for flow past hexagonal arrays of cylinders (Sangani and Acrivos, 1982a), and again show similar singular behavior as in square arrays of cylinders.

However, our approach is different, fully analytical, and covers the whole range of particle (solid) volume fraction with a single smooth function. The panel A in Fig. 11 shows that our new drag function represents both the dilute and dense flows, passes through the very dilute and dilute functions in Sangani and Acrivos (1982a), and at the same time, covers the entire spectrum of the solid volume fraction from fluid to dry limits in a well controlled manner. Importantly, our new model can be applied to rapid as well as slow flows of mixture materials, and for any Reynolds number. Furthermore, the new drag model also includes buoyancy effects, and the drag vanishes for the neutrally buoyant flows. This is a fundamental aspect of the mixture mass flows (Pitman and Le, 2005; Pudasaini, 2012). Our analytical solution is unified, a single solution covers the entire range of particle concentrations, from the fluid limit ($\alpha_s \to 0$: viscous flood) to dry limit ($\alpha_s \to 1$: landslide), and for any dilute to dense distribution of dispersed particles (debris flow). Moreover, drag vanishes at these limits as natural characteristics.

Furthermore, Durlofsky et al. (1987) presented numerical drag model (coefficient) for the sedimenting horizontal chains of uniformly-spaced identical spheres. However, essentially the drag is increasing very fast (exponential-like) as a function of number of spheres, so, number of dispersed particles, akin to the particle concentration in particle-fluid mixture. Yet, their drag coefficients can be obtained only after large computation of multi-body system with given applied force. Durlofsky et al. (1987) presented a discrete approach. We have developed a fundamentally novel continuum mechanics based fully analytical model for drag in mixture mass flow. So, our model is simple and much cheaper than the discrete models.

6. Application in debris flow simulation

To access the influence of the new full generalized drag (8) over the previous one (with $\mathscr{K} = 0$), here, we present some basic simulation results on benchmark debris flows. For this, we consider the general two-phase dynamical mass flow model of Pudasaini (2012). Further application of the new drag model can be found in Pudasaini and Mergili (2019).

6.1. Simulation set-up

For the simulations, we consider a typical set up of channel geometry and debris mass. The slope is inclined at an angle of 50°. The spatial domain for simulation ranges from $x = -50$ m to $x = 400$ m in the downstream direction, and from $y = -200$ m to $y = 200$ m in the

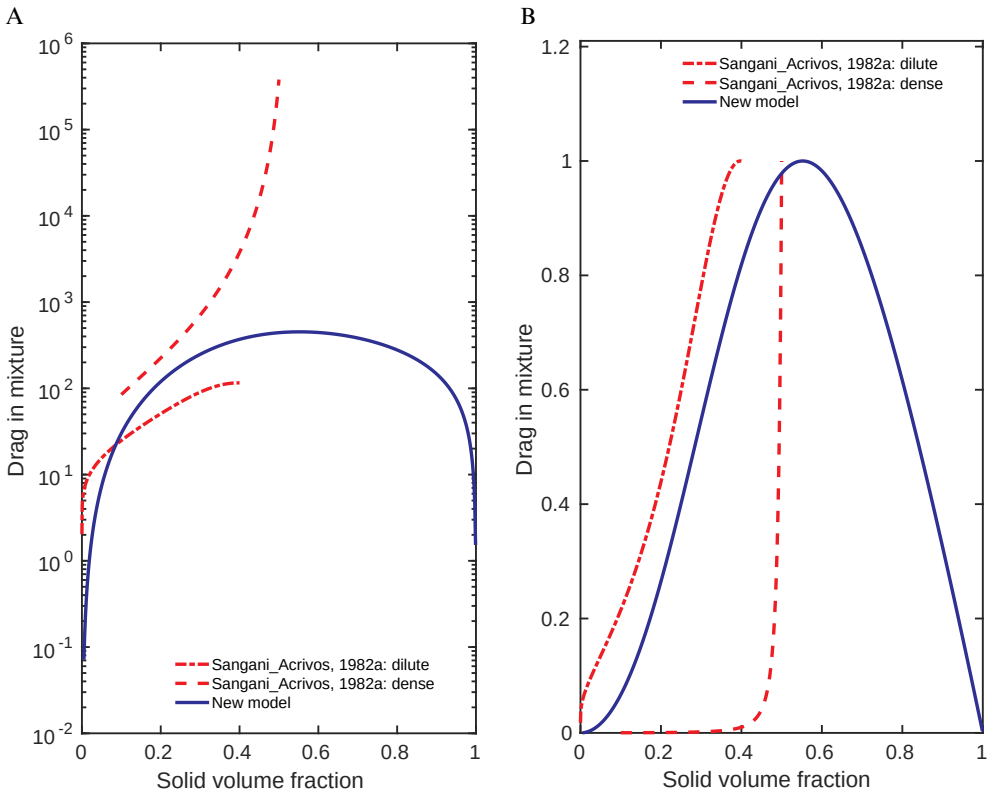

Fig. 11. Comparison between the drag model in Sangani and Acrivos (1982a) for square array of cylinders, and the new analytical model constructed here. A: lognormal; B: normalized plot with respect to the maximum of each functions in Sangani and Acrivos (1982a) and the new model.

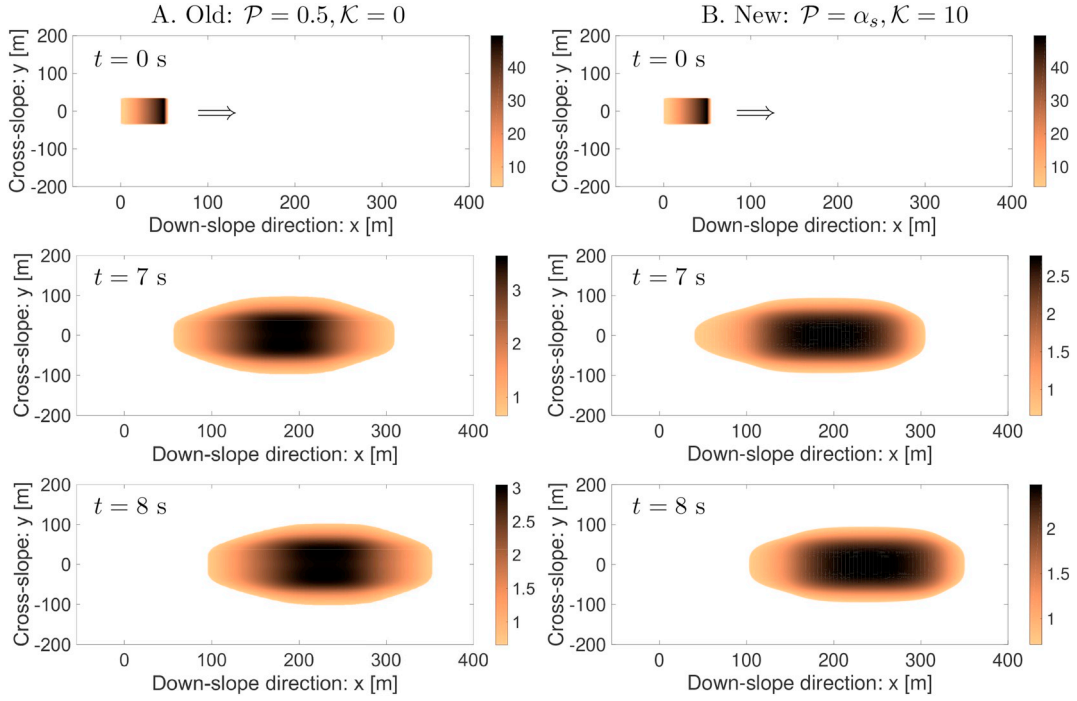

Fig. 12. Two-phase debris flow dynamics down an inclined surface (50°) indicating a developed flow. Initially ($t = 0$ s) the debris mixture consists of 65% solid, 35% fluid. A: with old model. B: with the new enhanced generalized drag (8). Color bars indicate flow depth in m. Arrows indicate the flow direction.

cross wise direction. The initial debris mass is defined by a triangular wedge 0 m $\leq x \leq$ 50 m, -35 m $\leq y \leq$ 35 m in Fig. 12 (top panels, $t = 0$ s) that contains a debris mixture of solid particles (65%) and viscous fluid (35%).

6.2. Simulation parameters

The Pudasaini (2012) model contains several physical parameters. The parameters chosen for the simulation (with proper dimensions) are: $\mathscr{W}_T = 1.0$, $Re_p = 1.0$; $\mathscr{P} = 0.5$, $\mathscr{K} = 0$ (for the previous model), or

$\mathscr{P} = \alpha_s$, $\mathscr{K} = 10$ (for the new model) as discussed earlier; $j = 1$, virtual mass $\mathscr{C} = 1.0$, quasi-Reynolds number $N_R = 30{,}000$, mobility Reynolds number $N_{R_A} = 1{,}000$, parameter indicating vertical distribution of the particle concentration $\xi = 3$, vertical shearing of fluid velocity $\chi = 5$, $\rho_s = 2700$, $\rho_f = 1100$, internal friction angle $\phi = 45^\circ$, and basal friction angle $\delta = 40^\circ$. These choices of parameters are made on the basis of the physics of two-phase mass flows (Pudasaini, 2012; Pudasaini, 2019; Pudasaini and Krautblatter, 2014; Kattel et al., 2016, 2018, and Mergili et al., 2017, 2018a, 2018b).

6.3. Numerical method

In order to capture the complicated phenomena of complex mixture mass flow, we employ high-resolution Total Variation Diminishing (TVD), Non-Oscillatory Central (NOC) schemes (Nessyahu and Tadmor, 1990; Jiang and Tadmor, 1998; Tai et al., 2002) to numerically integrate the Pudasaini (2012) model equations, with the previous and the new drag models. Such numerical schemes are efficient and have been extensively used in simple to sophisticated mass flow simulations (Pudasaini and Hutter, 2007; Mergili et al., 2017, 2018a, 2018b; Kattel et al., 2018; Qiao et al., 2019).

6.4. Simulation results

Panels A in Fig. 12 are the simulations with the previous model (with $\mathscr{P} = 0.5$, $\mathscr{K} = 0$), and panels B are the simulations with the new model (with $\mathscr{P} = \alpha_s$, $\mathscr{K} = 10$) given by (8), for time $t = 0{,}7{,}8$ s, respectively. This represents a type of fully developed flow. As the drag with $\mathscr{K} = 0$ is much higher in the local regions with substantial solid fraction, the major and the central portion of the debris body could not be fluidized or lubricated (due to unphysical access drag), and thus could not properly advect along the slope, even after 8 s. This resulted in the unphysically diffused front while the central region is resisted strongly due to the excess drag. However, with the new model ($\mathscr{K} \neq 0$) the drag is appropriately applied over the entire body (see, e.g., Fig. 2) that lets the debris mass to be properly fluidized allowing the substantial down-slope propagation of the major portion of the debris to the frontal part. This led to the formation of the frontal head as often observed in mixture debris flows (Kattel et al., 2016, 2018). A clear frontal head could not be developed in the simulation with the previous drag model. This resulted in the much different geometrical forms of the simulated debris bodies obtained with the previous and the new drag models.

The diffusive front (for $\mathscr{K} = 0$) is due to the very high initial hydraulic pressure at the front where the drag is comparatively low at the early stage of collapse and the incipient motion. However, in the main body, the hydraulic pressure is relatively low, so the drag is dominant there. This unphysically prevented the down-slope motion of the main body. But, for $\mathscr{K} \neq 0$, the drag is mild, also at the central part of the debris body, allowing the main body to legitimately accelerate down-slope due to gravity.

Another interesting point is the local distribution of the flow depth, which is much higher around the central portion of the debris body with the previous drag model ($h > 3.6$ m, and $h > 3$ m at $t = 7$ s and $t = 8$, respectively), while the flow depth is much less ($h \approx 2.7$ m, and $h \approx 2.5$ m at $t = 7$ s and $t = 8$, respectively), but more naturally distributed, with the new drag model. Similarly, the propagation speed of the major frontal head is quite slower with the previous model ($\mathscr{K} = 0$) at about $x = 235$ m, and $x = 280$ m, whereas this speed is much higher with the new drag model ($\mathscr{K} = 10$) at $x \approx 275$ m and $x \approx 325$ m at $t = 7$ s and $t = 8$, respectively. The difference between the surges with the old and new drag models is already about 40 m at $t = 7$ s, and 45 m at $t = 8$ s, respectively. These are big numbers even for the considered simulation configuration. Hence, the new enhanced generalized drag legitimately fluidizes (or lubricates) the debris mass leading to higher mobility. This is important to properly simulate the landslide motion and morphodynamics.

Furthermore, as the previous drag unphysically applies the higher resistance to the downslope motion, the debris mass in panel A is forced to expand more in the cross-slope direction, which is considerably less in panels B associated with the proper drag model. The maximum lateral extent in panels A at $t = 7$ s and $t = 8$ s are 200 m and 210 m at $x = 190$ m and $x = 240$ m, respectively. However, in panels B, the maximum lateral extent at $t = 7$ s and $t = 8$ s are 190 m and 195 m at $x = 200$ m and $x = 250$ m, respectively.

All these discrepancies with the previous drag model are due to the unnecessarily higher drag for considerable to higher solid volume fraction, which has now been removed by the new enhanced and full drag model. This sheds light on the basic mechanics and flow dynamics of the new drag model.

Further advantage of the new model is that, because of the singularity induced instability, the drag with $\mathscr{K} = 0$ requires much smaller CFL number than the CFL number for the simulation with $\mathscr{K} \neq 0$. This results in efficient flow simulation with the new drag. So, such a new smooth drag function is very advantageous in real applications with complex multi-phase mass flows and in combination with open source computational tool, e.g., the r.avaflow (Mergili et al., 2017; Qiao et al., 2019) that required to impose conditions on the old drag when it becomes unphysically large. Such conditions can now be lifted. This highlights the immediate application potential of the new drag model in real field scale landslide and debris flow events (Bout et al., 2018; Mergili et al., 2018a, 2018b; Zheng et al., 2018; Wang et al., 2019a; Wang et al., 2019b).

7. Discussions

We have compared the existing partial fluid-type (Pailha and Pouliquen, 2009), solid-type (Pitman and Le, 2005) and the full, new drag model in mixture mass flows. This revealed that the new model removes singularities in existing models. Furthermore, we compared our new model with different other hydrodynamic drag models. The numerical and analytical models in Sangani and Acrivos (1982a, 1982b) show fast increase of the drag forces for relatively higher volume fraction of the dispersive phase, and indicates the singular behavior. However, our approach is fully analytical, unified, behaves nicely, and a single solution covers the entire range of particle concentrations. The new model can be applied to fast and slow flows. We also compared our drag model with discrete numerical drag model of Durlofsky et al. (1987) which essentially shows fast increasing behavior as number of dispersed particle increases. Our efficient continuum mechanics based analytical model is valid for the whole range of particle concentration. Moreover, the mixture flow simulation sheds light on the basic mechanics and flow dynamics of the smooth, but strongly non-linear new enhanced generalized drag model. This offers a great first-ever opportunity to be applied to a wide range of mixture flow problems, including landslides and debris flows (Bout et al., 2018; Mergili et al., 2018b; Zheng et al., 2018; Qiao et al., 2019; Wang et al., 2019a; Wang et al., 2019b). Due to these important aspects, we now discuss the results on the new enhanced generalized drag in mixture mass flows mainly based on Fig. 7.

I. For all the choices of the exponent n in $\mathscr{P} = \alpha_s^n$; there is a common drag value of about $C_{DG} = 0.047$ at about $\alpha_s = 0.6$, akin to a saturation state. For $n = 1.0$, the mean value of $C_{DG} = 0.02$, which is the most often used empirical drag value in literature (Zwinger et al., 2003; Pudasaini and Hutter, 2007), but here obtained with the involvements of the underlying physical parameters and mechanical processes in mixture flows. As n deviates away from unity, two asymmetric families of drag curves emerge. However, the drags for $n \leq 1.0$ are probably the most suitable ones. In the new derivation (8), the function $\mathscr{P}$ is dynamically fixed and is no more a free parameter, so is $\mathscr{U}_T$. This substantially helps in simulation by

reducing the parameter uncertainties (Mergili et al., 2017, 2018a).

II. There are some special values of the solid volume fractions for which the drag takes maximum values and then, decrease on either side of that particular value of α_s. This is a strikingly new understanding and completely counter intuitive. But, this special behavior can be explained from a physical point of view: For this, we consider the family of drag curves for $n \leq 1$. As α_s increases from its lower values, C_{DG} also increases, first gently, then rapidly, but until a certain value that lies in (0.65, 0.75), a typical value of saturation. Then, it decreases rapidly as α_s tends to approach its right limit. Why is this meaningful? This is so, because as the debris material tends to the state of close packing, the drag behaves completely differently. To the value just lower than the dense packing, the drag quickly increases if more and more solid particles are added in to the system that increases the drag. Still, the fluid can pass through the inter-connected pores, so both the solid- and fluid-like drags are effective. But, if further grains are added in to the system then, the material tends to behave more like solid and the fluid effects are rapidly diminishing, because the fluid can not move relatively freely as it could do before. Furthermore, as the material is densely packed, grains are increasingly supported by the neighboring grains, and thus, cannot freely move in the fluid as before. The solid drag virtually tends to vanish as α_s tends to unity. So, effectively, both the solid and the fluid drags are decreasing after a certain peak value of the solid volume fraction in the mixture. Such decreasing drag with increasing α_s are also observed for churn-turbulent, and/or slug flows (Ishii and Chawla, 1979; Ishii and Hibiki, 2011) indicating that (8) with large α_s values may behave as churn or slug flows. For the churn-turbulent-flow regime, in which the radius of the fluid particle is further increased, and for the slug-flow regime, the volume of a bubble becomes very large, or equivalently, we can consider assembly of densely packed particles, whose shape can significantly deform to fit the channel geometry. Thus, the diameters of the bubbles, or the granular assembly ("particles") may become nearly that of the channel width with a thin liquid film separating such particles from the wall. As shown by Ishii and Chawla (1979), in these situations, the drag coefficient decreases with the increase in the volumetric concentration, and finally, the drag coefficient vanishes as the volumetric concentration of solid tends to unity.

III. The dynamics of C_{DG} as observed in Fig. 7 might be utilized to model the slug flow scenario. The curve connecting the maxima of the drag can be selected for this purpose. This curve has two maxima and a minimum in between. High drag means high resistance to flow, and vice versa. The slug flow could be developed in local areas where the drag is high, whereas the smooth and more dispersed flows can be developed in between in the local region of low drag. Thus, on the one hand, locally small or large n values, and small $\mathscr{K}$ and γ, all enhance the drag, and thus, possibly generate a favorable condition for the slug formation, a bit away on either side of the dense packing of the dispersed phase. On the other hand, intermediate n values and larger $\mathscr{K}$ and γ reduce the drag substantially close to the dense packing of the dispersive phase. So, by randomly, but appropriately, switching the mass flux intensity associated with n and $\mathscr{K}$, we might be able to generate a slug flow.

IV. The most important aspect of the new drag function is that, for any value of α_s, C_{DG} is sufficiently smooth and behaves nicely in contrast to the previous models where they tend to show infinitely large value of C_{DG} for sufficiently large value of the solid volume fraction (Ganatos et al., 1978; Ishii and Chawla, 1979; Sangani and Acrivos, 1982a, 1982b; Durlofsky et al., 1987; Ni and Beckermann, 1991; Pitman and Le, 2005; Pailha and Pouliquen, 2009; Ishii and Hibiki, 2011; Pudasaini, 2012). So, the new model removes the singularity, or nonphysically rapidly increasing value of the drag with the solid volume fraction.

V. The mixture flow dynamics is influenced by the solid (or, the fluid) fraction if it is sufficiently bounded away from zero. Otherwise, the dynamics is not substantially altered by the solid (or, the fluid) phase (Pudasaini, 2012). So, in practice, very small and very large values of the solid fractions can be technically ignored. As suggested by (1) or (8), generally in the limit as α_s or α_f tends to zero, C_{DG} should vanish. This is a natural requirement because, in these limits, the material behaves as if it was a single-phase material (Pudasaini and Hutter, 2007). So, virtually no drag contribution should appear as the origin of the drag is the non-zero relative velocity between the solid and the fluid phases.

VI. The drag force can be applied for both the unstructured and structured flows. For relatively high solid contents, but unstructured flows with negligible cohesive bonds between grains, the drag coefficient might be more accurate. However, the drag force decreases with the structured flow. This can be explained with the new drag force, with reference to Fig. 7. For example, consider $n = 1$. Structured matrix can be assumed with substantially higher solid fraction. As α_s becomes larger than a typical dense packing, say $\alpha_s > 0.65$, the drag decreases rapidly and finally becomes zero as α_s tends to the solid limit ($\alpha_s \to 1$), the fully structured state of the material.

However, the performance and the suitability of the new drag model should be checked with laboratory data and field events. Further parameter sensitivity analysis should be performed for the parameter M appearing in solid-type drag contribution, and j which is associated with the laminar- and turbulent-type drag. The drift factor λ appearing in the mass flux contribution, $\mathscr{K}$, should also be calibrated that models whether the solid or the fluid phase moves faster. This signifies whether the frontal surge is solid- or fluid-dominated, depending on $\lambda < 1$, or $\lambda > 1$, or the flow behaves as if it was a homogeneous mixture ($\lambda = 1$) of solid particles and viscous fluid.

8. Summary

Based on the first principle, we have analytically derived an enhanced generalized drag in mixture mass flows that fully describes the drag for any values of the solid volume fraction. The new drag model incorporates the contribution due to the mass flux that was neglected in previous formulations. We have constructed functional relations for the new contributions and parameters appearing in the model connecting them with the solid volume fraction, and the mass flux. The previous formulation was restricted to the regions where velocities are relatively small. That produced singularity in the drag for large values of the solid volume fraction. In existing dispersive mixture mass flow and hydrodynamic drag models, drag can tend to unrealistically large value and tend to infinity as the solid volume fraction becomes higher, or approaches unity. Our new model removes such singularity inherited by existing models.

There are several important implications of the enhanced generalized drag combined with the functional values and parameters depending on dense to dilute distribution of particles in the mixture that strongly determine the shape and the magnitude of the drag curve, characterizing the new extended model. One of the most striking points is that, for the reasonably selected parameter values, the mean value of the enhanced generalized drag appeared to be the often used value in literature but, without any physical justification. We have provided a full analytical solution and physical basis for the dynamically evolving complex drag in the mixture flow with well-posed behavior. The further physically important point is: For some special value of the solid volume fraction, the drag takes its maximum. This is a strikingly new understanding. The drag increases for the larger values of the solid volume fraction, which, however, decreases for the lower values of the solid volume fraction. However, the drag must decrease after a certain value of the solid fraction. This has been explained. The most important aspect of the new drag function is that, for any value of the solid

fraction, the drag is sufficiently smooth. Depending on the nature of the mixture, from dilute to dense flows, two fundamentally different families of generally asymmetrical drag curves emerge. We have identified the physically most suitable drag curves. A benchmark simulation of debris flow clearly indicates the application potential of the new drag model in real field events. We have shown that better knowledge of evolving mixture, from dilute to dense, and thus the evolving solid fraction is very important for the proper understanding of the drag, and thus, the flow dynamics as a whole. So, the new analytical, smooth and strongly non-linear enhanced drag offers a great opportunity for the full dynamical simulation of a wide range of mixture mass flows including, landslides and debris flows.

Acknowledgements

We gratefully acknowledge the financial support provided by the German Research Foundation (DFG) through the research project, PU 386/5-1: “A novel and unified solution to multi-phase mass flows”: U_MultiSol.

References

Absi, R., 2005. Comment on turbulent diffusion of momentum and suspended particles: a finite-mixing-length theory. Phys. Fluids 17, 079101. https://doi.org/10.1063/1.1949200.
Bout, B., Lombardo, L., van Westen, C.J., Jetten, V.G., 2018. Integration of two-phase solid fluid equations in a catchment model for flashfloods, debris flows and shallow slope failures. Environ. Model. Softw. 105, 1–16.
Bossis, G., Brady, J.F., 1984. Dynamic simulation of sheared suspensions. I. General method. J. Chem. Phys. 80, 5141–5154.
Brennan, D., 2001. The numerical simulation of two-phase flows in settling tanks. In: PhD Thesis. University of London.
Brennen, C.E., 1982. A Review of Added Mass and Fluid Internal Forces. Naval Civil Engineering Laboratory, Port Hueneme, California (CA 93043. Report Number: CR 82.010).
Brennen, C.E., 2005. Fundamentals of Multiphase Flows. Cambridge University Press (ISBN 0521 848040).
Cook, T.L., Harlow, F.H., 1984. Virtual mass in multiphase flow. Int. J. Multiphase Flow 10, 691–696.
de Haas, T., Braat, L., Leuven, J.R.F.W., Lokhorst, I.R., Kleinhans, M.R., 2015. Effects of debris flow composition on runout, depositional mechanisms, and deposit morphology in laboratory experiments. J. Geophys. Res. 120, 1949–1972.
Drew, D.A., 1983. Mathematical modelling of two-phase flow. Annu. Rev. Fluid Mech. 15, 261–291.
Durlofsky, L., Brady, J.F., Bossis, G., 1987. Dynamic simulation of hydrodynamically interacting particles. J. Fluid Mech. 180, 21–49.
Ganatos, P., Pfeffer, R., Weinbaum, S., 1978. A numerical-solution technique for three-dimensional Stokes flows, with application to the motion of strongly interacting spheres in a plane. J. Fluid Mech. 84, 79–111.
Han, Z., Wang, W., Li, Y., Huang, J., Su, B., Tang, C., Chen, G., Qu, X., 2018. An integrated method for rapid estimation of the valley incision by debris flows. Eng. Geol. 232, 34–45.
He, C., Hu, X., Tannant, D.D., Tan, F., Zhang, Y., Zhang, H., 2018. Response of a landslide to reservoir impoundment in model tests. Eng. Geol. 247, 84–93.
Hiltunen, K., Jaesberg, A., Kallio, S., Karema, H., Kataja, M., Koponen, A., Manninen, M., Taivassalo, V., 2009. Multiphase Flow Dynamics. Theory and Numerics. [Monifaasivirtausten dynamiikka. Teoriaa ja numeriikkaa]. Espoo 2009. VTT Publications, pp. 722.
Hsu, T.-W., Chang, H.-K., Hsieh, C.-M., 2003. A two-phase flow model of wave-induced sheet flow. J. Hydraul. Res. 41, 299–310.
Ishii, M., Chawla, T.C., 1979. Local Drag Laws in Dispersed Two-phase Flow. Argonne National Lab. Report, ANL-79-105.
Ishii, M., Mishima, K., 1984. Two-fluid model and hydrodynamic constitutive relations. Nucl. Eng. Des. 82, 107–126.
Ishii, M., Hibiki, T., 2011. Thermo-Fluid Dynamics of Two-Phase Flow, Second edition. Springer, New York, USA.
Jakobsen, H.A., Sannaes, B.H., Grevskott, S., Svendsen, H.F., 1997. Modeling of vertical bubble-driven flows. Ind. Eng. Chem. Res. 36, 4052–4074.
Jiang, G.S., Tadmor, E., 1998. Non-oscillatory central schemes for multi-dimensional hyperbolic conservation laws. SIAM J. Sci. Comput. 19, 1892–1917.
Kafle, J., Pokhrel, P.R., Khattri, K.B., Kattel, P., Tuladhar, B.M., Pudasaini, S.P., 2016. Landslide-generated tsunami and particle transport in mountain lakes and reservoirs. Ann. Glaciol. 57 (71), 232–244.
Kafle, J., Kattel, P., Mergili, M., Fischer, J.-T., Pudasaini, S.P., 2019. Dynamic response of submarine obstacles to two-phase landslide and tsunami impact on reservoirs. Acta Mech. 230 (9), 3143–3169.
Kattel, P., Khattri, K.B., Pokhrel, P.R., Kafle, J., Tuladhar, B.M., Pudasaini, S.P., 2016. Simulating glacial lake outburst floods with a two-phase mass flow model. Ann. Glaciol. 57 (71), 349–358.
Kattel, P., Kafle, J., Fischer, J.-T., Mergili, M., Tuladar, B.M., Pudasaini, S.P., 2018. Interaction of two-phase debris flow with obstacles. Eng. Geol. 242, 197–217.
Kendoush, A.A., 2008. Hydrodynamic solution of the virtual mass coefficient of a vortex ring moving in a fluid. Ind. Eng. Chem. Res. 47, 1081–1084.
Khattri, K.B., Pudasaini, S.P., 2018. An extended quasi two-phase mass flow model. Int. J. Non-Linear Mech. 106, 205–222.
Kolev, N.I., 2007. Multiphase Flow Dynamics 2: Thermal and Mechanical Interactions. Springer.
Kowalski, J., 2008. Two-phase modeling of debris flows. PhD Thesis. ETH, Zurich, Switzerland.
Luca, I., Tai, Y.-C., Kuo, C.-Y., 2015. Shallow Geophysical Mass Flows Down Arbitrary Topography: Model Equations in Topography-Fitted Coordinates, Numerical Simulation and Back-Calculation of Disastrous Events. Springer.
Manninen, M., Taivassalo, V., Kallio, S., 1996. On the Mixture Model for Multiphase Flow. Espoo, Technical Research Center of Finland. VTT Publications 288 (ISBN 951-38-4946-5; ISSN 1235-0621).
Mergili, M., Fischer, J.-T., Krenn, J., Pudasaini, S.P., 2017. r.avaflow v1, an advanced open-source computational framework for the propagation and interaction of two-phase mass flow. Geosci. Model Dev. 10, 553–569.
Mergili, M., Emmer, A., Juricova, A., Cochachin, A., Fischer, J.-T., Huggel, C., Pudasaini, S.P., 2018a. How well can we simulate complex hydro-geomorphic process chains? The 2012 multi-lake outburst flood in the Santa Cruz Valley (Cordillera Blanca, Peru). Earth Surf. Process. Landf. 43, 1373–1389.
Mergili, M., Frank, B., Fischer, J.-T., Huggel, C., Pudasaini, S.P., 2018b. Computational experiments on the 1962 and 1970 landslide events at Huascarn (Peru) with r.avaflow: lessons learned for predictive mass flow simulations. Geomorphology 322, 15–28.
Nessyahu, H., Tadmor, E., 1990. Non-oscillatory central differencing for hyperbolic conservation laws. J. Comput. Phys. 87 (2), 408–463.
Ni, J., Beckermann, C., 1991. A volume-averaged two-phase model for transport phenomena during solidification. Metall. Trans. B 22B, 349–361.
Pailha, M., Pouliquen, O., 2009. A two-phase flow description of the initiation of underwater granular avalanches. J. Fluid Mech. 633, 115–135.
Pitman, E.B., Le, L., 2005. A two fluid model for avalanche and debris flows. Phil. Trans. R. Soc. A 363 (3), 1573–1601.
Pokhrel, P.R., Khattri, K.B., Tuladhar, B.M., Pudasaini, S.P., 2018. A generalized quasi two-phase bulk mixture model for mass flow. Int. J. Non-Linear Mecha. 99, 229–239.
Pudasaini, S.P., 2012. A general two-phase debris flow model. J. Geophys. Res. 117, F03010.
Pudasaini, S.P., 2019. A fully analytical model for virtual mass force in mixture flows. Int. J. Multiphase Flow 113, 142–152.
Pudasaini, S.P., Hutter, K., 2007. Avalanche Dynamics: Dynamics of Rapid Flows of Dense Granular Avalanches. Springer, Berlin, New York.
Pudasaini, S.P., Krautblatter, M., 2014. A two-phase mechanical model for rock-ice avalanches. J. Geophys. Res. Earth Surf. 119, 2272–2290.
Pudasaini, S.P., Mergili, M., 2019. A multi-phase mass flow model. J. Geophys. Res. https://doi.org/10.1029/2019JF005204.
Pudasaini, S.P., Fischer, J.-T., 2016a. A mechanical erosion model for two-phase mass flows. arXiv: 1610.01806.
Pudasaini, S.P., Fischer, J.-T., 2016b. A mechanical model for phase-separation in debris flow. arXiv: 1610.03649.
Qiao, C., Ou, G., Pan, H., 2019. Numerical modelling of the long runout character of 2015 Shenzhen landslide with a general two-phase mass flow model. Bull. Eng. Geol. Environ. 78, 3281–3294.
Ren, Z., Wang, K., Yang, K., Zhou, Z.H., Tang, Y.J., Tian, L., Xu, Z.-M., 2018. The grain size distribution and composition of the Touzhai rock avalanche deposit in Yunnan, China. Eng. Geol. 234, 97–111.
Richardson, J.F., Zaki, W.N., 1954. Sedimentation and fluidization: Part 1. Trans. Inst. Chem. Eng. 32, 35–53.
Sangani, A.S., Acrivos, A., 1982a. Slow flow past periodic arrays of cylinders with Application to heat transfer. Int. J. Multiphase Flow 8, 193–206.
Sangani, A.S., Acrivos, A., 1982b. Slow flow through a periodic arrays of spheres. Int. J. Multiphase Flow 8, 343–360.
Tai, Y.-C., Noelle, S., Gray, J.M.N.T., Hutter, K., 2002. Shock-capturing and front tracking methods for granular avalanches. J. Comput. Phys. 175 (1), 269–301.
Wang, L., Zaniboni, F., Tinti, S., Zhang, X., 2019a. Reconstruction of the 1783 Scilla landslide, Italy: numerical investigations on the flow-like behaviour of landslides. Landslides 16, 1065–1076.
Wang, F., Wang, J., Chen, X., Chen, J., 2019b. The influence of temporal and spatial variations on phase separation in debris flow deposition. Landslides 16, 497–514.
Yang, H.Q., Xing, S.G., Wang, Q., Li, Z., 2018. Model test on the entrainment phenomenon and energy conversion mechanism of flow-like landslides. Eng. Geol. 239, 119–125.
Zhang, M., Yin, Y., 2013. Dynamics, mobility-controlling factors and transport mechanisms of rapid long-runout rock avalanches in China. Eng. Geol. 167, 37–58.
Zheng, H.C., Shi, Z.M., Peng, M., Yu, S.B., 2018. Coupled CFD-DEM model for the direct numerical simulation of sediment bed erosion by viscous shear flow. Eng. Geol. 245, 309–321.
Zwinger, T., Kluwick, A., Sampl, P., 2003. Numerical simulation of dry-snow avalanche flow over natural terrain. In: Hutter, K., Kirchner, N. (Eds.), Dynamic Response of Granular and Porous Materials under Large and Catastrophic Deformations, Lecture Notes in Appl. and Comput. Mech. vol. 11. Springer, Berlin, pp. 161–194.